



## Article

# Assessment of a Top and Bottom Cooling Strategy for Prismatic Lithium-Ion Cells Intended for Automotive Use <sup>†</sup>

Said Madaoui <sup>1,2</sup> , Bartłomiej Guzowski <sup>3</sup> , Roman Gozdur <sup>3</sup> , Zlatina Dimitrova <sup>1</sup>, Nicolas Audiot <sup>1</sup>, Jocelyn Sabatier <sup>2,\*</sup> , Jean-Michel Vinassa <sup>2</sup> and Franck Guillemard <sup>1</sup>

<sup>1</sup> Stellantis, 2 bd Europe, 78300 Poissy, France; said.madaoui@u-bordeaux.fr (S.M.); zlatina.dimitrova@stellantis.com (Z.D.); nicolas.audiot@stellantis.com (N.A.); franck.guillemard@stellantis.com (F.G.)

<sup>2</sup> IMS Laboratory, University of Bordeaux, CNRS, Bordeaux INP, IMS, UMR 5218, 33400 Talence, France; jean-michel.vinassa@ims-bordeaux.fr

<sup>3</sup> Department of Semiconductor and Optoelectronic Devices, Lodz University of Technology, Politechniki 10, 93-590 Lodz, Poland; bartłomiej.guzowski@p.lodz.pl (B.G.); roman.gozdur@p.lodz.pl (R.G.)

\* Correspondence: jocelyn.sabatier@u-bordeaux.fr; Tel.: +33-540-006-540

<sup>†</sup> The present work is an extension of the paper “Evaluation of Dual Side Cooling System for Prismatic Batteries for Vehicle Applications” presented at the 36th International Conference on Efficiency, Cost, Optimization, Simulation and Environmental Impact of Energy Systems (ECOS 2023) and published online in Proceedings.com.



**Citation:** Madaoui, S.; Guzowski, B.; Gozdur, R.; Dimitrova, Z.; Audiot, N.; Sabatier, J.; Vinassa, J.-M.; Guillemard, F. Assessment of a Top and Bottom Cooling Strategy for Prismatic Lithium-Ion Cells Intended for Automotive Use. *Batteries* **2024**, *10*, 403. <https://doi.org/10.3390/batteries10110403>

Academic Editor: Federico Baronti

Received: 5 October 2024

Revised: 3 November 2024

Accepted: 7 November 2024

Published: 15 November 2024



**Copyright:** © 2024 by the authors. Licensee MDPI, Basel, Switzerland. This article is an open access article distributed under the terms and conditions of the Creative Commons Attribution (CC BY) license (<https://creativecommons.org/licenses/by/4.0/>).

**Abstract:** In contemporary vehicle applications, lithium-ion batteries have become a leading option among the diverse array of battery technologies available. This preference is attributed to their advantageous properties, which include low self-discharge rates and no memory effect. Despite these benefits, lithium-ion batteries are not without their challenges. The key issues include a restricted driving range, concerns regarding longevity, safety risks, and prolonged charging durations. Efforts aimed at minimizing the charging duration frequently entail the introduction of elevated currents into the battery, a practice that can significantly elevate its temperature and, in turn, diminish its operational lifespan. Generally, battery packs in electric vehicles are equipped with flat cooling plates located on their side or bottom surfaces, which also serve the dual purpose of providing heating in colder conditions. Nevertheless, this cooling configuration faces difficulties during fast charging and may not efficiently heat or cool the batteries. In this work, a novel thermal management approach is proposed, in which a battery module is cooled not only with a bottom cooling plate but also using another cooling plate in contact with the busbars, located on the top of the battery module. The simulations and experimental tests show that this new configuration demonstrates significant improvements. The thermal time constant is reduced by 47%, enabling faster cooling of the module. Additionally, the maximum temperature reached by the battery during charging with dual cooling is lowered by 6 °C compared to the conventional approach. In this configuration, the top cooling plate acts as a thermal bridge. This is a key advantage that promotes temperature homogenization within the battery module. As a result, it supports an even aging process of batteries, ensuring their longevity and optimal performance.

**Keywords:** Li-ion batteries; electric vehicle; thermal gradient; thermal management; cooling plates

## 1. Introduction

In electric vehicles, the battery module is the exclusive and principal energy source. Nevertheless, in order to establish electric cars as a feasible substitute for those powered by internal combustion engines, engineers and experts must tackle numerous technical obstacles. These obstacles mainly focus on improving a vehicle’s range and extending battery life, in addition to minimizing charging durations. Lithium-ion batteries have progressively developed from various technological foundations. Their high energy density,

low self-discharge rate, and absence of a memory effect have transformed energy storage technology and facilitated the mobile revolution [1].

Lithium-ion batteries are produced in various configurations and shapes, such as prismatic, cylindrical, and pouch cells. The temperature significantly influences both the performance and longevity of a battery pack. Fluctuations in temperature within lithium-ion batteries result in varying rates of electrochemical reactions. According to Arrhenius' law, elevated temperatures enhance the speed of these electrochemical processes, which in turn increase the state of charge (SOC) due to the more rapid intercalation of lithium ions into the electrode material. This temperature-induced variation in the SOC and thermal gradient can thus lead to uneven distributions of the current density, localized differences in the SOC, and variations in the aging rate across a battery. The effects of the thermal gradient on battery degradation and lifespan reduction were analysed in detail in [2,3]. The thermal gradient not only hastens the overall aging of a battery but also reduces the amount of usable energy. Managing temperature increases and minimizing the spatial temperature gradients within a battery are the critical thermal challenges encountered during fast charging [4].

Battery thermal management systems (BTMS) are widely utilized in contemporary vehicles to address various thermal challenges [5]. A mere 5 °C fluctuation in the temperature can lead to a decrease in the capacity of a battery pack by approximately 1.5–2%, while its power output may diminish by as much as 10% [6,7]. In an effort to enhance the cooling efficiency of lithium-ion batteries, researchers have explored a range of cooling methodologies. Currently, air cooling, liquid cooling, and phase-change materials are commonly employed for effective battery thermal management. Other cooling solutions are also under investigation [8]. Depending on their budgetary constraints and/or specific technical requirements, manufacturers of battery packs may opt for one or a combination of these cooling strategies. Thermal management systems (TMS) can be categorized into two main types: active and passive cooling. While active cooling systems require additional energy for the operation of pumps and fans, they generally offer greater efficiency compared to passive cooling solutions [9].

Active liquid cooling techniques can be categorized into indirect-contact and direct-contact methods. Indirect cooling typically employs a mixture of water and ethylene glycol to mitigate the risk of freezing within the cooling plates, whereas direct cooling necessitates the use of a dielectric liquid to avert short-circuiting. Although there is an increasing interest in direct-contact cooling due to its superior efficiency [10], automotive manufacturers continue to prefer indirect liquid cooling solutions. When designing a cooling plate, several critical factors must be considered: (a) ensuring that the battery temperature remains within the manufacturer's specified operational range, (b) effectively dissipating the maximum heat generated by the batteries during thermal runaway events, (c) minimizing both the weight and size of the TMS, (d) reducing the coolant pressure drop within the cooling plate, [11]. Furthermore, the indirect cooling technique fulfils a dual function by both cooling and preheating batteries in low-temperature environments. This method is advantageous as the cooling plate can effectively transfer heat to the batteries, thereby facilitating their preheating when necessary. In cold-weather scenarios, preheating the battery of an electric vehicle is essential for optimizing its performance and extending its lifespan. This preheating can be accomplished through either external or internal heating strategies [12,13]. A battery model consists of both electrical and thermal elements. In terms of the electrical model, there are primarily two approaches with which to represent a lithium-ion cell: a physics-based model and an Equivalent-Circuit Network (ECN) model.

The physics-based model introduced by Newman, for example, employs partial differential equations to incorporate both the temporal and spatial dimensions, thereby effectively illustrating the various internal mechanisms at work within a cell. While this model is both accurate and adaptable, its intricate computational requirements pose challenges for integration into existing management algorithms [14]. In contrast, Wang et al. [15] proposed a more straightforward discrete electrochemical model that is applicable across a broad

temperature spectrum. Building on Newman's framework, the ECN models represent a second approach that simulates battery behaviour by likening it to an electrical circuit. These models utilize localized constants, which negate the necessity for spatial dimensions, resulting in equations that are ordinary differential equations reliant solely on time [16]. The complexity of these models varies, but they are primarily designed for an in-depth analysis of the overall electrothermal performance of a battery cell. Despite significant progress in battery modelling and thermal management, several critical issues remain unresolved: (a) there is a scarcity of literature focused on reducing the thermal gradient within batteries through a combination of experimental and simulation approaches, and (b) limited research has investigated the benefits of heat extraction via busbars with a cooling plate placed atop the battery module.

The principal objective of this research is to evaluate the function of a top cooling plate in the thermal regulation of a battery module. To fulfil this objective, this investigation emphasizes a series of experimental tests on a battery module, contrasting the thermal management effectiveness of two cooling technologies: bottom cooling and dual cooling. Additionally, this study involves the development and calibration of a model based on the data obtained from these experimental tests, which are utilized to examine various scenarios under extreme conditions, including high current and convection forces. Through these efforts, this research seeks to offer significant insights into the impact of a top cooling plate on temperature fluctuations within a battery and the overall efficiency of thermal management. The structure of this paper is as follows: it begins with a review of the model presented in a prior publication [17], which concentrated on the development and validation of a lithium-ion cell model. Subsequently, it details the modelling strategy for a battery module consisting of 12 interconnected cells via busbars, including information on the model's calibration. The next section describes the test bench employed to validate the proposed model, on which various tests were performed and compared to the module's electrothermal model. The analysis includes both bottom cooling and dual cooling configurations in terms of their cooling efficiency. This paper concludes with a comprehensive summary and reflections on potential directions for future research.

## 2. Li-Ion Batteries Electrothermal Modelling

A fundamental aspect of creating battery prognostics solutions involves the development of a battery model. A model allows automotive manufacturers to simulate battery performance and analyse battery-related problems in a manner that is comprehensible to both users and designers [18].

### 2.1. Model of the Battery Module

The battery module under investigation comprises 12 prismatic cells. As illustrated in Figure 1a, they are interconnected via busbars to create a 3p4s configuration. To ensure the precise modelling of the battery module, a comprehensive approach is adopted, which entails the modelling of each individual cell and its components, as shown in Figure 1b,c. This section presents the developed model.

Electrothermal modelling is a widely utilized approach among various battery modelling techniques, aimed at exploring the relationship between the current flowing through a battery and its temperature. This modelling framework integrates electrical and thermal models in a cohesive manner. The primary inputs for the electrical model include the discharge current, state of charge (SOC), and temperature. These inputs are instrumental in generating heat within the thermal model, which subsequently yields a temperature output signal. This temperature signal is then reintroduced into the electrical model to assess its impact on the electrical parameters, such as internal resistance. Typically, the heat generated by a battery, denoted as  $Q_{gen}$ , during both the charging and discharging processes, comprises two components: reversible and irreversible heat [19], which can be mathematically represented by Equation (1). The entropy change is responsible for the reversible heat,  $Q_{rev}$ , which can be expressed by (2), while the irreversible heat,  $Q_{irr}$ ,

corresponds to the heat produced by ohmic resistance and is expressed by (3). The electrical model is taken in a receiver convention, i.e.,  $I > 0$ , during the charging process [20].

$$Q_{gen} = Q_{irr} + Q_{rev} \quad (1)$$

$$Q_{rev} = IT_b \frac{\partial OCV}{\partial T_b} \quad (2)$$

$$Q_{irr} = I^2 R \quad (3)$$

where the current delivered or supplied to the battery is represented by  $I$ , while  $R$  denotes the internal resistance of the battery. The battery temperature is denoted by  $T_b$ . Irreversible heat comes from different sources, such as ohmic losses due to electron/ion transport and the overpotential from electrochemical reactions. This type of heat is always positive. Interestingly, about 80% of the total heat generated during battery operation comes from reaction heat. On the other hand, reversible heat is related to changes in entropy caused by phase transitions in electrode materials driven by electrochemical reactions. Its sign changes based on the battery's SOC and the direction of the current flow [21]. To prevent the accumulation of heat within a cell, the heat is typically exchanged with neighbouring elements through conduction (represented by  $Q_{cond}$ ) or dissipated through convection (represented by  $Q_{dis}$ ). These two modes of heat exchange are expressed by (4) and (5), respectively.

$$Q_{cond} = \frac{T_{neigh} - T_b}{R_{th}} \quad (4)$$

$$Q_{dis} = h_{conv} (T_{env} - T_b) \quad (5)$$

where  $h_{conv}$  is the heat transfer coefficient,  $T_{env}$  denotes the ambient temperature, and  $T_{neigh}$  indicates the temperature of the neighboring elements surrounding the battery cell. The battery cell temperature is influenced by multiple heat transfer paths. To maintain the battery temperature in a reasonable range, it is essential to dissipate a portion of the generated heat to the external environment. This process prevents heat accumulation and effectively reduces the temperature rise [22].

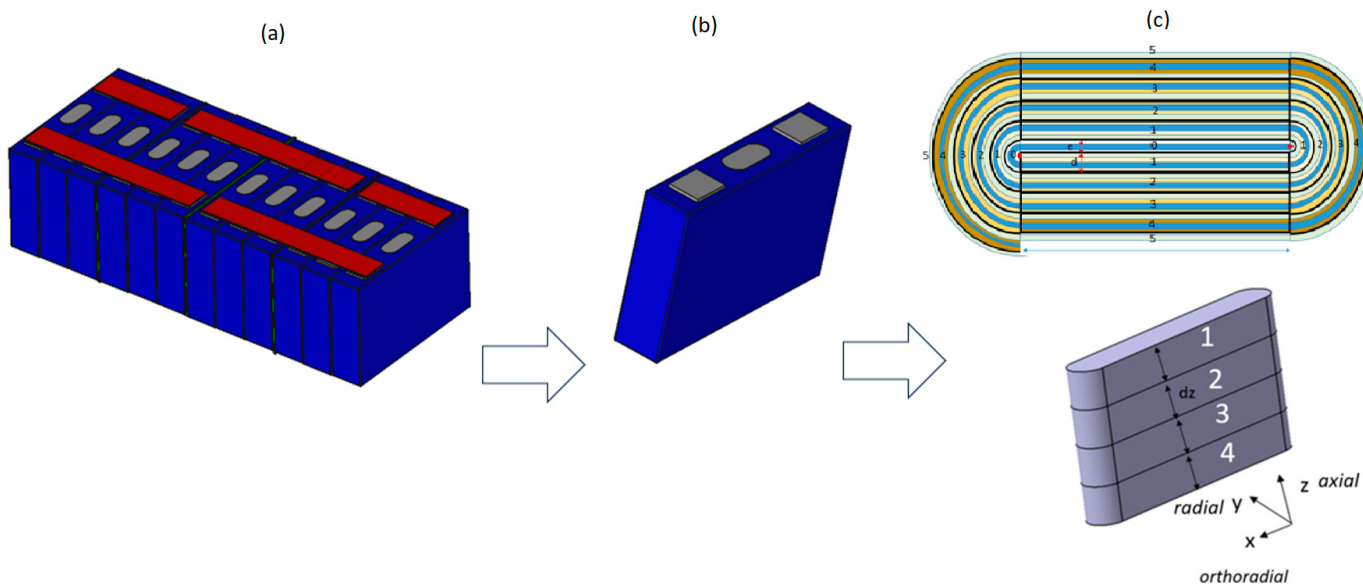


**Figure 1.** The structure of the studied system: (a) the battery module, (b) the battery cell, and (c) the jelly roll mesh [23].

In this study, the device of interest is a commercial 67 Ah prismatic Li-ion cell. The battery cell specifications are presented in Table 1. Since a detailed description and validation of the cell model are provided in [17], only the key points are highlighted here.

**Table 1.** Battery cell specifications.

Specification	Value
Cathode material	NMC
Anode material	Graphite
Nominal capacity	67 [Ah]
Cut-off voltages	2.8–4.2 [V]
Dimensions	150–30–100 [mm]
Thermal conductivities	40–2.5–40 [ $\text{W}\cdot\text{m}^{-1}\cdot\text{K}^{-1}$ ]
Specific heat capacity	1200 [ $\text{J}\cdot\text{kg}^{-1}\cdot\text{K}^{-1}$ ]

The battery cell is a complex system consisting of various components, including jelly rolls (abbreviated as JRs and also called the electrode assembly), a casing, a cover, and insulating films. In order to develop a comprehensive model of the cell, both the JRs and the casing are considered during the modelling process. With this approach, the thermal response of the battery can be accurately depicted, indicating the temperature responses of both the internal and external points within the cell. The following section describes the modelling methods for the JRs and casing.

### 2.1.1. JR Modelling

To date, various models have been built and a wide range of work focusing on the thermal modelling of lithium-ion batteries has been reported. The simplest and most common approach is to treat a cell as a homogenous and isotropic material. The limitation of this approach is that it does not provide internal thermal gradients, due to the isotropic assumption. On the other hand, there are more complex models based on a Finite Element Analysis (FEA) with a detailed cell structure that can reach a very high accuracy, but the complexity of these models greatly limits their real-time application. In the available literature, there are optimal models that are efficient, and which consider the material anisotropy while being capable of assessing the inner thermal gradient. However, these models are currently limited to cylindrical cells and do not encompass prismatic cells [24]. In this study, the primary aim is to effectively visualize and quantify the temperature gradients within cells using a simulation model that can be seamlessly integrated into an electric vehicle. Given the complex geometry of a JR, it is essential to employ a well-designed mesh to accurately represent the heat exchanges in all directions within a cell. The proposed model uses a meshing technique that considers both the thickness and the height of the JR. Importantly, this mesh design includes the orthoradial direction, facilitating heat exchange between the meshes as the heat traverses around the windings. In Figure 2, the proposed mesh is illustrated, considering three directions: the axial (along the JR's height, z), radial (perpendicular to the winding, y), and orthoradial (parallel to the winding, x) [25]. This comprehensive meshing approach differentiates this model from those in the existing literature and contributes to a more accurate representation of the heat transfer phenomena within a JR.

A JR is obtained by wrapping electrodes around a hollow space. Each turn is qualified as an elementary layer that is made up of different sub-layers (cathode, anode, separator, and current collectors). Each individual sub-layer possesses a distinct thermal conductivity, capacity, thickness, and density. The JR model is fully detailed in [17], with all the equations that represent the physics at the JR level.

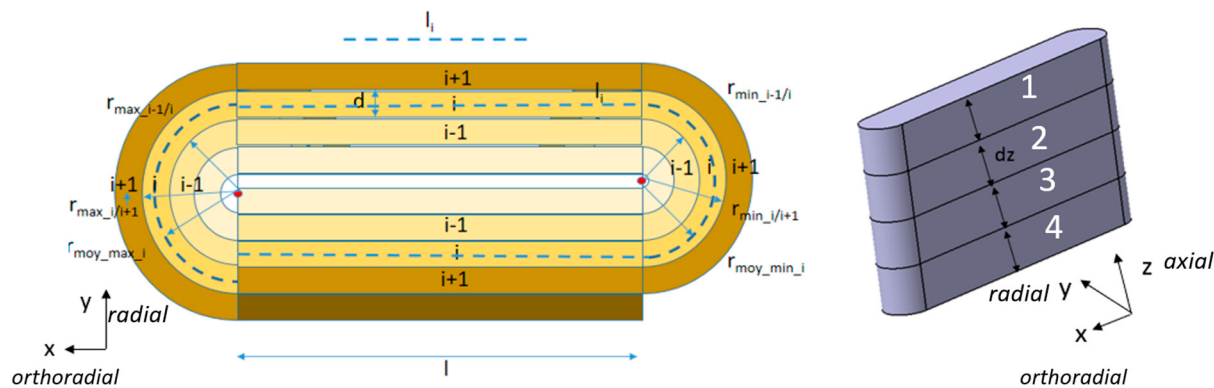


**Figure 2.** The proposed mesh of the JR [23].

To summarize, the heat generated by a mesh  $i, j$  can be calculated according to the following equation:

$$Q_{i,j} = R_{30s\ i,j} I^2_{i,j} + I_{i,j} T_{i,j} \frac{\partial OCV_{i,j}}{\partial T_{i,j}} \quad (6)$$

in which  $Q_{i,j}$  denotes the total heat generated by the individual mesh  $i, j$ , while  $R_{30s\ i,j}$  denotes the electrical resistance of mesh  $i, j$  that contributes to the irreversible heat generation. Additionally,  $I_{i,j}$  denotes the electrical current delivered by mesh  $i, j$ , and  $T_{i,j}$  refers to the temperature of mesh  $i, j$ .

### 2.1.2. Casing Modelling

The casing of lithium-ion batteries plays a crucial role, as it is the primary source of thermal and mechanical protection for the JR. It must endure various stresses while remaining lightweight and easy to manufacture. Typically, casings are crafted from extruded aluminium tubes with laser-welded endcaps [26]. To create a thorough model of a cell, it is essential to incorporate the JR with its surrounding components, beginning with the casing, which serves as a thermal bridge linking the JR to the external environment. To illustrate the thermal gradient on the casing, it is divided into meshes along its height, with each mesh  $j$  of the casing linked to a corresponding mesh  $i, j$  of the JR. Given that the casing is constructed from aluminum, its specific properties have been well established in the literature [27].

### 2.1.3. Busbar Modelling

The busbar modelling approach involves segmenting the busbar into individual meshes, where each mesh is governed by the differential equation

$$m_{BBi} C_{BB} \frac{dT_{BBi}}{dt} = Q_{generation} + Q_{convection} + Q_{conduction}. \quad (7)$$

In relation (7),  $C_{BB}$  denotes the specific heat capacity of the busbar, and  $m_{BBi}$  is the mass of a specific mesh  $i, j$  within the busbar. Additionally,  $Q_{convection}$  denotes the heat lost through either forced or natural convection, and  $Q_{conduction}$  represents the heat transfer that occurs between the busbar meshes as well as between the busbar mesh and the cell terminals.  $Q_{generation}$  refers to the heat generated mostly by the Joule effect, according to

$$Q_{generation} = \frac{\rho l_{BBi}}{S_{BBi}} I^2 \quad (8)$$

where  $\rho$  represents the busbar material density,  $l_{BBi}$  is the length of each busbar mesh, and  $S_{BBi}$  denotes the cross-sectional area of the busbar. Within the module, two types of busbars are used: long busbars that link six cells, and short busbars that connect three cells. Therefore, the long busbar is divided into six meshes, while the short busbar is divided

into three meshes, with each mesh connected to a cell terminal. Figure 3 illustrates an example of the meshing of a busbar consisting of three meshes, where  $BB_i$  represents the central mesh.

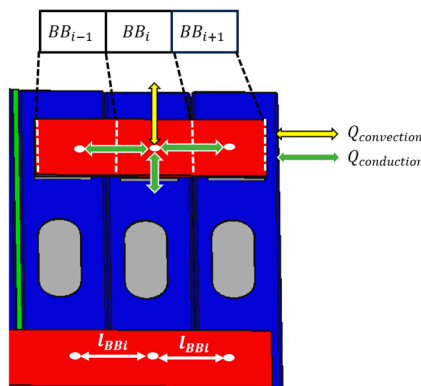


**Figure 3.** Meshed busbar connecting 4 cells in parallel.

The linkage of battery cells presents both electrical and mechanical challenges. These linkages can be established through a range of joining technologies. The choice of joining technologies has a considerable effect on the performance, capacity, and longevity of a battery pack [28,29].

## 2.2. Model Calibration

After establishing the cell model, it was replicated twelve times to create the 3p4s module model. Consequently, the battery module consists of four groups, with each group containing three cells. These cells within a set are thermally connected via the busbars and their casings. After building a set of three cells, each set was replicated four times, by assuming uniform cell properties. These four sets were then thermally interconnected through busbars, forming the 3p4s battery module. Prior to initiating the module model calibration, a number of assumptions were established.

### 2.2.1. Assumptions

The following assumptions were considered:

- All the cells within the module are identical.
- The thermal spacers positioned between the cell sets indicate that the sole thermal conduction route between the sets is through the busbars.
- The air temperature within the climate chamber and of the liquid circulating through the cooling plates are maintained at a constant level during the entire test.
- The model's initial and boundary conditions are considered suitable for the experimental circumstances.

### 2.2.2. Battery Module Without Any Cooling Plate

To calibrate the previously mentioned model, a series of electrothermal experiments were carried out on the 3p4s battery module. Initially, these experiments were conducted on the module without a cooling plate, as illustrated in Figure 4a, with the aim of accurately replicating the thermal and electrical responses of all twelve cells. The battery module was situated within a climate chamber during these experiments. The first parameter to be assessed was the heat exchange coefficient ( $h_{conv}$ ). The second parameter involved the contact electrical resistance between the electrical load and the terminals of the battery module. These contact electrical resistances significantly affect the thermal behaviour of the batteries, particularly when the contact is suboptimal. The calibrated convection coefficient was obtained after fitting an experimental curve whose value was  $15 \text{ [W}\cdot\text{m}^{-1}\cdot\text{K}^{-1}]$ , and the contact resistance value was considered negligible due to the ultrasonic welding technology

used for connecting the busbar to the tab. This approach ensured that the model accurately replicated the thermal behaviours of both the busbars and the cells.

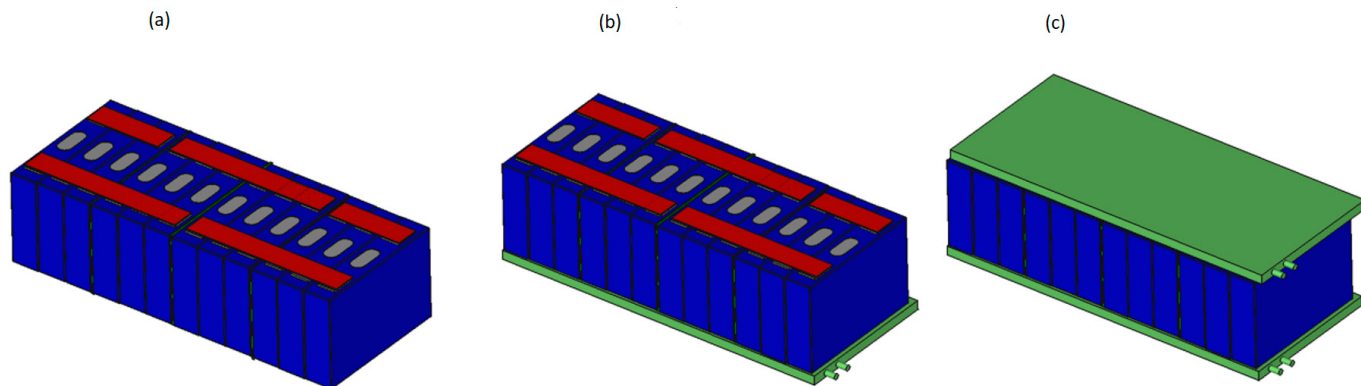


**Figure 4.** Battery module thermal management with three different configurations: (a) a module that lacks a cooling plate; (b) a module featuring a cooling plate at the bottom; and (c) a module equipped with a cooling plate at the top and bottom [23].

### 2.2.3. Battery Module with Top and Bottom Cooling Plates

The battery module undergoes the same electrothermal tests in two different configurations. Initially, the battery module is connected with only a bottom cooling plate (as illustrated in Figure 4b), followed by coupling the battery module with both bottom and top cooling plates (as depicted in Figure 4c). K-type thermocouples, with a diameter of 0.3 mm, are used for the data acquisition. These thermocouples offer an accuracy of  $\pm 1.5$  °C and a time response of 0.7 s. The instrumentation is designed to evaluate the advantages of incorporating cooling plates and to subsequently analyze the technologies regarding their thermal management efficiency. At the model level, the sole parameters required to accurately replicate the thermal responses of the cells are (a) the thermal resistance between the bottom cooling plate and the lower surfaces of the cells for the initial scenario, and (b) the thermal resistance between the upper cooling plate and the busbars for the subsequent scenario, according to

$$R_{th\ tot} = R_{th\ TI} + R_{th\ CP}. \quad (9)$$

In this relationship, the total thermal resistance, denoted as  $R_{th\ tot}$ , represents the overall thermal resistance between a cooling plate and the battery module.  $R_{th\ CP}$  refers to the thermal resistance attributed to the cooling plate, while  $R_{th\ TI}$  represents the resistance attributed to the thermal interface between the cooling plate and the cell. Both resistances,  $R_{th\ TI}$  and  $R_{th\ CP}$ , are calculated, respectively, using the following equations:

$$R_{th\ TI} = \frac{e}{\lambda S} \quad (10)$$

$$R_{th\ CP} = \frac{1}{h S}. \quad (11)$$

The connection between the battery module and the cooling plates is achieved using thermal interfaces to ensure good thermal contact and effective electrical insulation. The thermal interface between the busbars and the top plate is provided by GLPOLY's XK-P20 thermal pad (Shenzhen, China), characterized by a thermal conductivity of  $2$  [ $\text{W}\cdot\text{m}^{-1}\cdot\text{K}^{-1}$ ]. The thermal interface between the lower surface of the module and the bottom cooling plate is achieved using Saint-Gobain's TC2005 thermal pad (La Defense, France), which has a conductivity of  $1.6$  [ $\text{W}\cdot\text{m}^{-1}\cdot\text{K}^{-1}$ ].

Figure 5 depicts the thermal pathways connecting the cooling plates to a cell within the battery module. This illustration emphasizes the contact surfaces taken into account for the calculation of the thermal resistances arising from the thermal interfaces, specifically

between the upper plate and the busbars (denoted as  $R_{th\ TI\ 1}$ ) and between the lower plate and the bottom surface of the cell casing (denoted as  $R_{th\ TI\ 2}$ ).

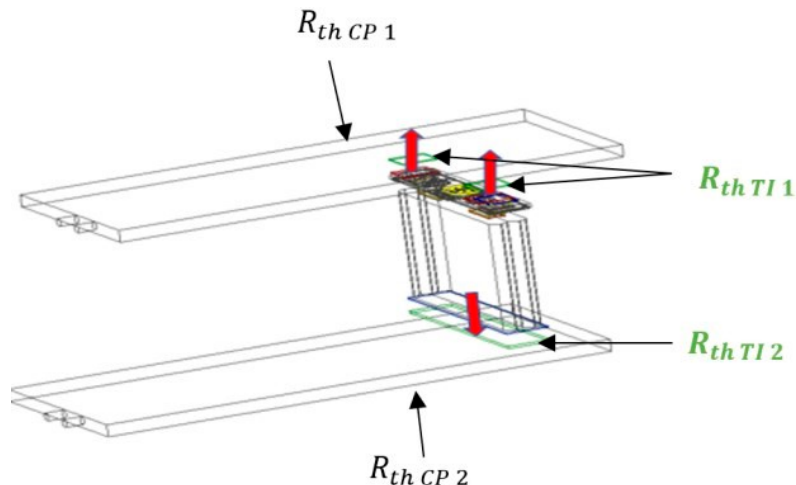


**Figure 5.** The thermal paths between the cooling plates and a cell in the battery module.

Given the heat dissipation towards both cooling plates, as illustrated by the red arrows in Figure 5, and applying (10), the values of the thermal resistances are determined and they are as follows: 6 K/W for  $R_{th\ TI\ 1}$  and 0.6 K/W for  $R_{th\ TI\ 2}$ . The thermal resistances  $R_{th\ CP\ 1}$  and  $R_{th\ CP\ 2}$  are calibrated using the electrothermal tests outlined in Section 2. Initially, the value of  $R_{th\ CP\ 2}$  is derived from the tests performed on the module equipped with only the bottom cooling plate, whereas  $R_{th\ CP\ 1}$  is obtained after conducting the same tests on the module with both bottom and top cooling plates. After adjustment, the numerical values found for these resistances are 10 K/W for  $R_{th\ CP\ 1}$  and 30 K/W for  $R_{th\ CP\ 2}$ .

### 3. Configuration of Measurement Apparatus and Testing Protocols

#### 3.1. Battery Module Tested

The absence of a direct interaction between the jelly roll and the cell terminals raised questions regarding the efficiency of the heat extraction from the upper part of the cells. This section aims to explore and evaluate the advantages of incorporating a top cooling plate into the thermal management system of the battery.

The technical specifications of the cells were previously presented, while the details pertaining to the battery module examined in this section are provided in Table 2.

**Table 2.** Rated parameters of the tested battery module.

Parameter	Nominal Value
Capacity	201 [Ah]
Rated module voltage	14.6 [V]
Min module voltage	11.2 [V]
Max module voltage	16.8 [V]
1C charge/discharge current	201 [A]

#### 3.1.1. Thermal Control System and Thermal Test Protocol

The experimental configuration includes a thermal management system that consists of two cooling plates, a water chiller, and a thermal chamber. As illustrated in Figure 6, the battery module is situated within the thermal chamber. The lower cooling plate is connected in parallel to the upper cooling plate and is supplied with water from the CW-6100AN chiller. This chiller is responsible for controlling the inlet temperature of the purified water.

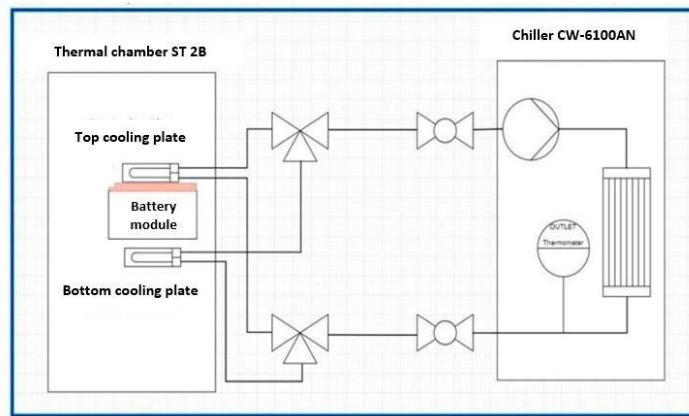


**Figure 6.** A schematic diagram illustrating the thermal management system employed for the tests [23].

Figure 7 shows the battery module with both the bottom and top plates mounted on it within the thermal chamber.

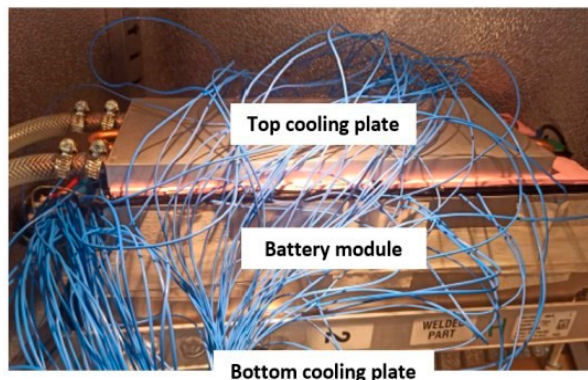


**Figure 7.** Battery module with bottom and top cooling plates.

### 3.1.2. Charging/Discharging System and Procedures

Figure 8 describes the test bench used for the calibration and analysis of the module model. Two power supplies (TDK Lambda GEN60-85-3P300 (TDK Lambda, Les Ulis, France) and ITECH IT6533 (ITECH, Nanjing, China)) were used to maximize the charge and discharge currents. As the electronic load, an EA-ELR 9080 unit was used. The charge and discharge were activated/deactivated with LEV200A4ANA relays (TE Connectivity, Schaffhouse, Switzerland). The multimeter used was a Keithley DAQ6510 (Keithley Instruments, Solon, OH, USA) with a 7706 module. To measure the current, an LEM LF510S current sensor (LEM International SA, Meyrin, Switzerland) was used. To measure the temperature inside the module, 45 K-type thermocouples were used, and four additional K-type thermocouples were used to measure the temperature inside the climatic chamber.

The uncertainties associated with the equipment used are listed in detail in Table 3. This table provides a comprehensive view of the sources of uncertainty, highlighting the specific aspects of the equipment that can influence the results or measurements obtained during the experiments.

A software-controlled test bench, shown in Figure 9, was used to replicate specific discharge and charge cycles. To control the SOC during the charging tests, two high-power supplies operating in Constant Current (CC) and Constant Voltage (CV) modes were employed. The discharging process was handled by an Electronic Load EA-ELR 9080. Throughout these tests, the battery voltage, charging/discharging currents, and temperature were recorded using over 45 thermocouples.

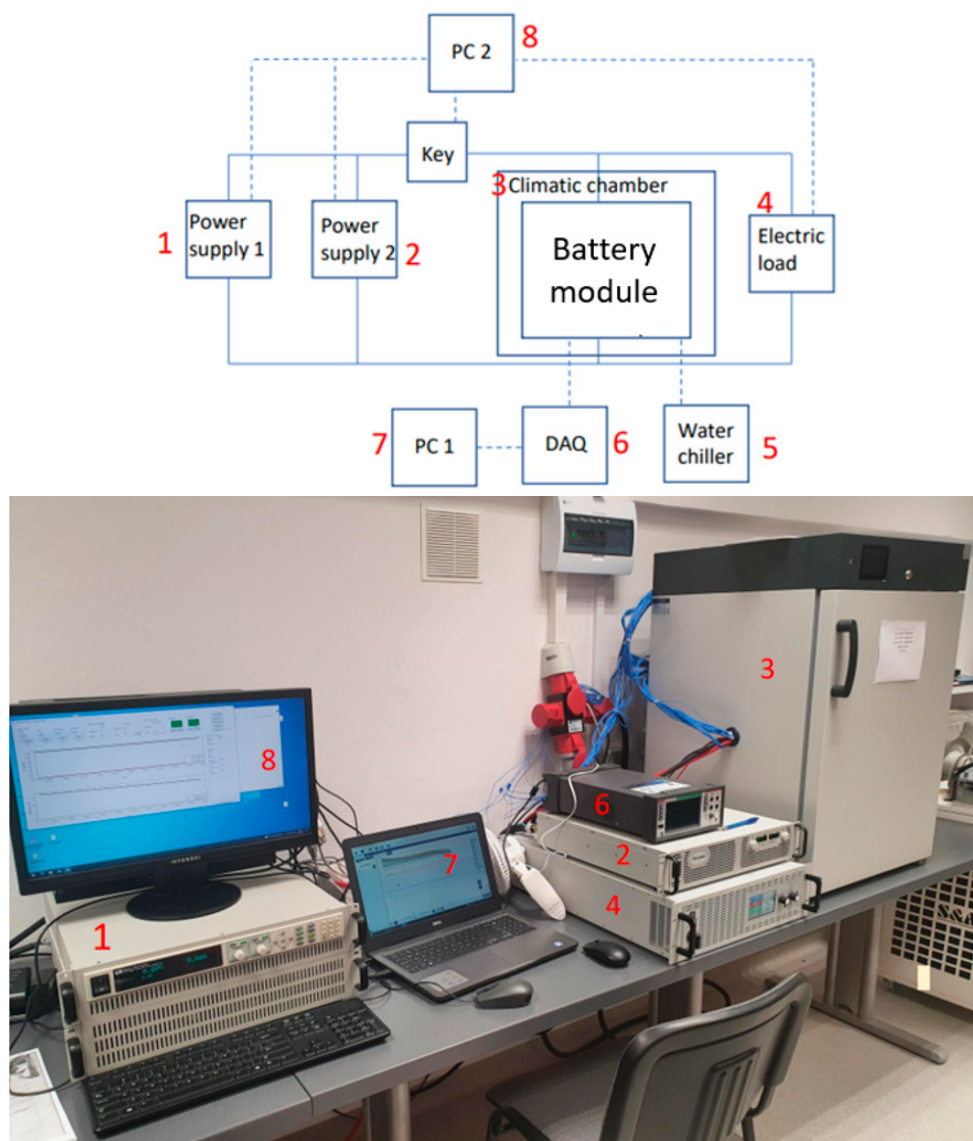


**Figure 8.** Schematic representation (up) and picture (down) of the test bench.

**Table 3.** Uncertainties related to equipment used in electrothermal tests.

Equipment	Uncertainties
Power supply ITECH IT6533 Max 200VDC/120A/6kW (ITECH, Nanjing, China)	Voltage: <0.05% + 100 mV; Current: <0.2% + 120 mA
Power supply TDK-LAMBDA GEN60-85 Max 60VDC/85A (TDK Lambda, Les Ulis, France)	Voltage: <0.015% + 5 mV; Current: <0.1%
Data acquisition system Keithley DAQ 6510+40 (Keithley Instruments, Solon, OH, USA)	±1 °C
Electronic load Elektro-Automatik EA-ELR 9080 Max 80VDC/510A/10.5kW (EA ELEKTRO-AUTOMATIK GMBH, Viersen, Germany)	Voltage: <0.3%; Current: <0.4%
Climatic chamber ST 2B SMART POL-EKO Apertura (POL-EKO, Wodzisław Śląski, Poland)	<±0.8 °C
Chiller CW-6100AN (TEYU ELECTROMECHANICAL CO., Guangzhou, China)	±0.5 °C
45 Type K thermocouples (RS Pro, Beauvais, France)	±0.9 °C

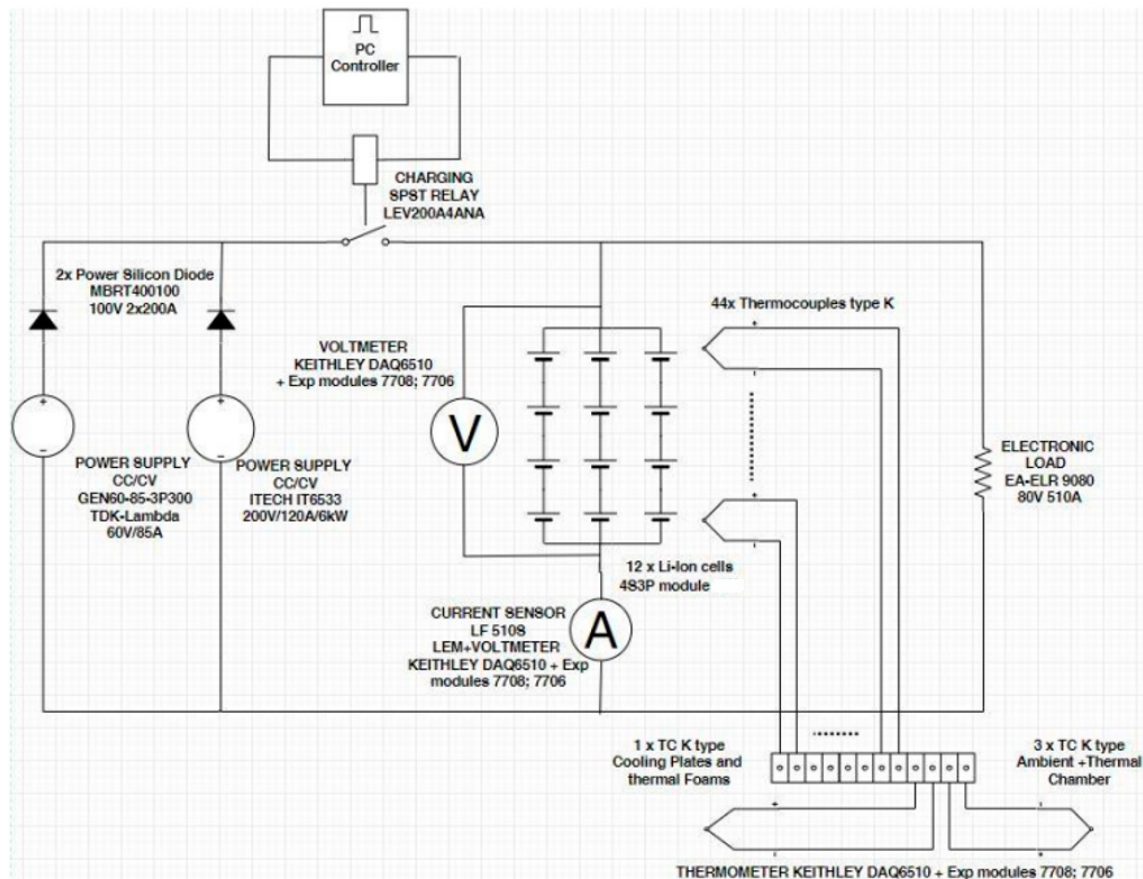


**Figure 9.** Schematic diagram of the integrated power devices responsible for controlling the state of charge.

Measurements were taken every 60 s using a Keithley DAQ6510 switching multimeter (Keithley Instruments, Solon, OH, USA), equipped with 7708 and 7706 expansion modules. This sampling interval was selected as a balance between accurately capturing the system behaviour and preventing data overload, given the use of over 40 sensors. It is important to note that the thermal time constants of the system were approximately 4000 s (as discussed later), resulting in a ratio of about 60 between the sampling interval and the system's time constants. This ratio ensured a reliable representation of the thermal phenomena.

The initial current profile, outlined in Figure 10, consisted of a controlled charging cycle divided into 5 stages. Each stage was carefully managed and triggered by a specific SOC, corresponding to a predetermined voltage of the battery module during the charging process. Before each charging cycle, the battery underwent a 100% Deep of Discharge (DoD) state [30]. The second type of electrothermal tests, shown in Figure 11, involved a two-stage discharge of the battery module at constant power values (2.6 kW discharge for 10 min followed by 2.3 kW discharge for 47 min) [31]. Before each discharging cycle, the battery underwent a 100% SOC.

The current profiles were chosen to analyse the battery's electrical and thermal behaviour, as its SOC varied during charging and discharging. These profiles also provided insight into how different current intensities influenced the battery's temperature.

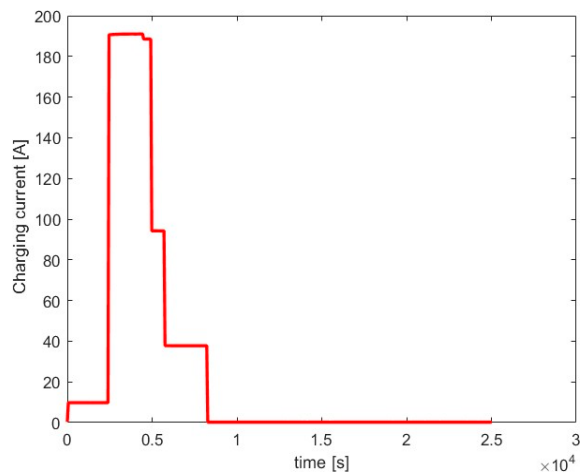


**Figure 10.** Charging current profile.

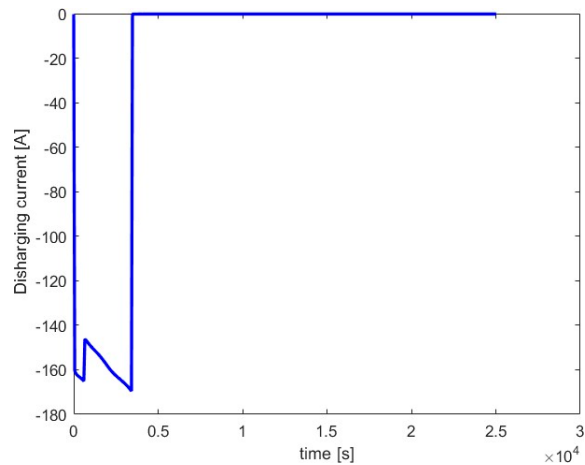


**Figure 11.** Discharging current profile.

#### 4. Experimental Results

##### 4.1. Battery Module During Charging

The thermal behaviour of the battery module was assessed during the charging test, with the coolant temperature maintained at  $T_c = 20\text{ }^\circ\text{C}$  and the ambient temperature at  $T_A = 25\text{ }^\circ\text{C}$ . To facilitate the analysis of the results and to examine the thermal gradients within the cell, along with the temperatures of the internal and external busbars, the subsequent analysis will utilize data from a limited number of thermocouples, as depicted in Figure 12. It should be noted that sensors 43, 44 and 45 are not visible in Figure 13, because they are located on the face opposite to that carrying sensors 40, 41 and 42.

The thermal behaviour of the battery module equipped solely with a bottom cooling plate during the charging test is illustrated in Figure 13.

The cooling process using only a bottom cooling plate had a time constant of  $\tau = 5700\text{ s}$ . The highest temperatures were observed at the terminals of the tested module due to poor electrical contact between the cell terminals and the busbars connecting the battery module to the power supply. The maximum temperature detected by the sensors located within the battery module, specifically sensor 19, sensor 20, and sensor 21, reached  $37\text{ }^\circ\text{C}$ , which is  $6\text{ }^\circ\text{C}$  lower than the temperature observed during the test that utilized only a bottom cooling plate. The temperature recorded on the side walls of the battery module remained below  $33\text{ }^\circ\text{C}$ . The implementation of an additional top cooling plate resulted in a reduction in the peak temperatures measured at the terminals, which were recorded at  $44\text{ }^\circ\text{C}$  (sensor 37) and  $35\text{ }^\circ\text{C}$  (sensor 38). The temperature difference between the busbar and the cell can be attributed to the difference in their specific heat capacities. The busbar, having a

lower thermal mass, was more responsive to changes in the external temperature, also leading to a quicker temperature variation compared to the cell. Moreover, to obtain comparison quantities, we called the “time constant” in the sequel; the time required for the temperature response to reach 50% of the variation to return to the ambient temperature after the first current pulse. The incorporation of a top cooling plate resulted in a 44% reduction in the cooling time constant, decreasing from  $\tau = 5700$  s to  $\tau = 3180$  s, as illustrated in Figure 13. As shown in Figure 14, the introduction of a top cooling plate offered another significant benefit: a reduced temperature variation within the battery module, which will be elaborated upon in Section 5 through extrapolations and an analysis only permitted by using the model. Therefore, the aging process of the batteries inside the battery module can be easily controlled.

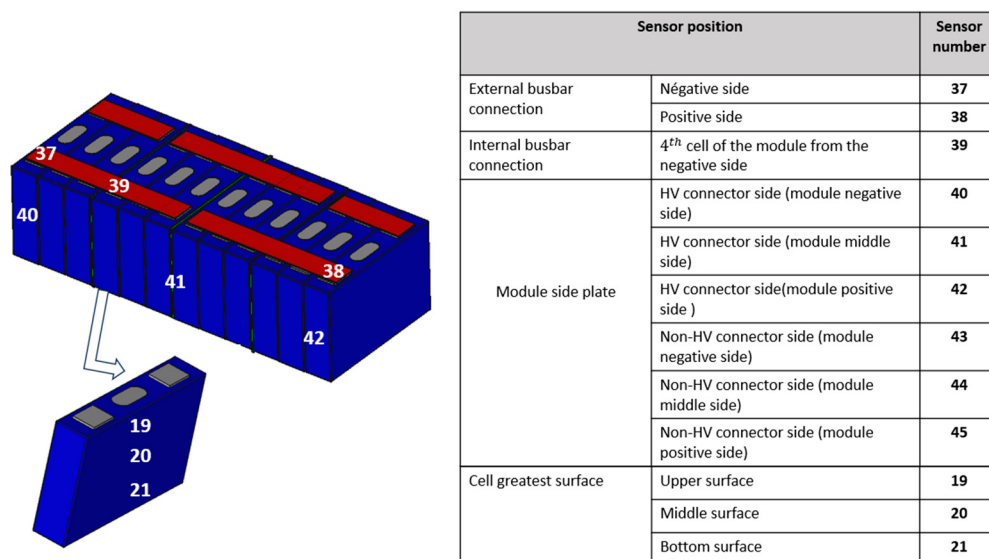


**Figure 12.** Temperature sensor layout [23] (sensors 43, 44 and 45 are not visible in the figure as they are located on the face opposite to that carrying sensors 40, 41 and 42).

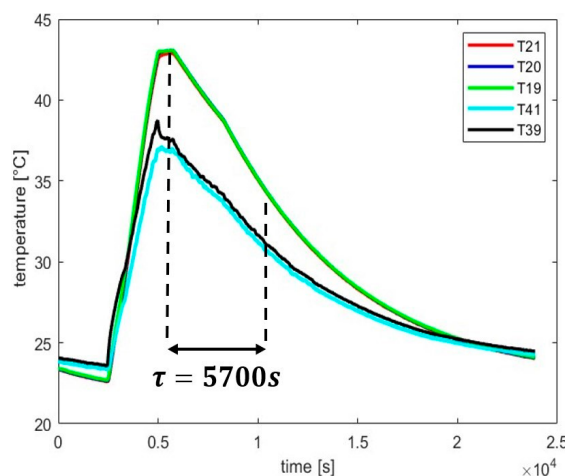


**Figure 13.** The thermal behaviour of the battery module with bottom cooling while charging (blue and red lines are covered by the green one).

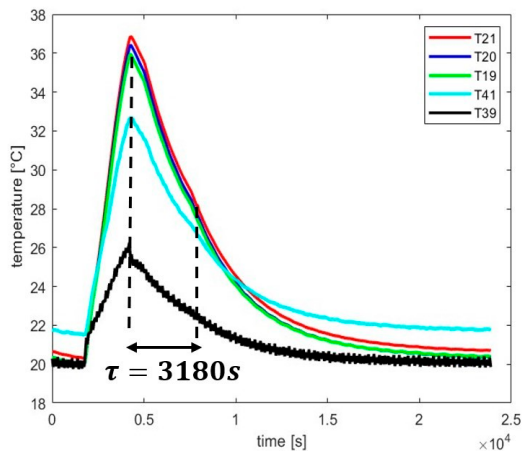


**Figure 14.** The thermal behaviour of the battery module with dual cooling while charging.

The most significant enhancement, amounting to 37%, was observed for sensor 38, which was located at one of the terminals. The average relative improvement inside the battery module was around 19%. The relative improvement rate of each thermocouple was calculated using the following equation:

$$RIR = \frac{(T_{\max BC} - T_{\min BC}) - (T_{\max DC} - T_{\min DC})}{T_{\max BC} - T_{\min BC}} \quad (12)$$

where  $T_{\max BC}$  refers to the maximum temperature recorded by the thermocouple during bottom cooling,  $T_{\min BC}$  denotes the minimum temperature recorded by the thermocouple during bottom cooling,  $T_{\max DC}$  corresponds to the maximum temperature recorded by the thermocouple during dual cooling, and  $T_{\min DC}$  indicates the minimum temperature recorded by the thermocouple during dual cooling.

#### 4.2. Discharging Battery Module

In addition to the charging tests, a discharge test was performed on the battery module at  $T_A = 25^\circ\text{C}$  and  $T_C = 30^\circ\text{C}$ . The same test was conducted on the module that was fitted with both bottom and top cooling plates. Figure 15 shows the module's thermal behaviour during battery discharge with bottom cooling.

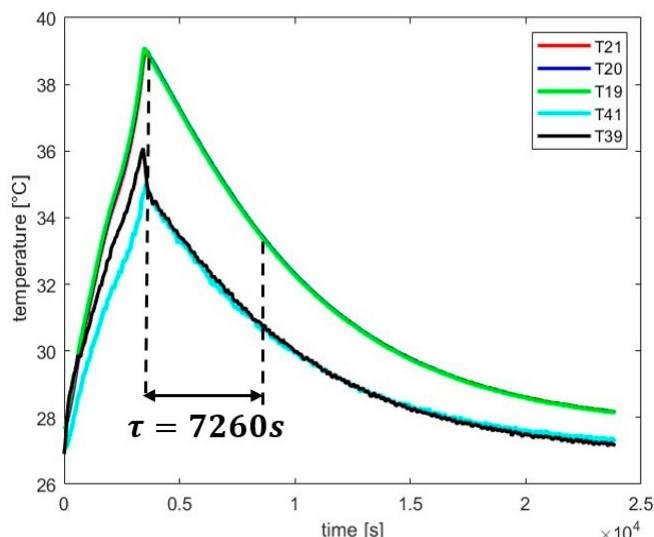


**Figure 15.** The thermal behaviour of the battery module with bottom cooling while discharging (blue and red lines are covered by the green one).

The variations in the C-rate profile resulted in an extended time constant for the cooling process, measured at  $\tau = 7260$  s during battery discharge and 5700 s during battery charge. In this case study, the time constant was reduced by 55% in the tests utilizing two cooling plates. The maximum temperatures recorded at the terminals of the battery module before and after the addition of the top cooling plate were 45 °C and 43 °C, respectively. Following the integration of the top plate, the maximum temperature decreased by 2 °C; however, the temperature distribution within the module became more uniform when both top and bottom cooling plates were employed. At  $t = 6000$  s, the temperature difference between the interior of the battery module and the external walls was halved, decreasing from 5 °C to 2.5 °C. The average relative improvement rate was calculated to be 31%. Additionally, the temperature of the busbar (sensor 39) decreased by 3 °C after the top cooling plate was added, as illustrated in Figure 16.

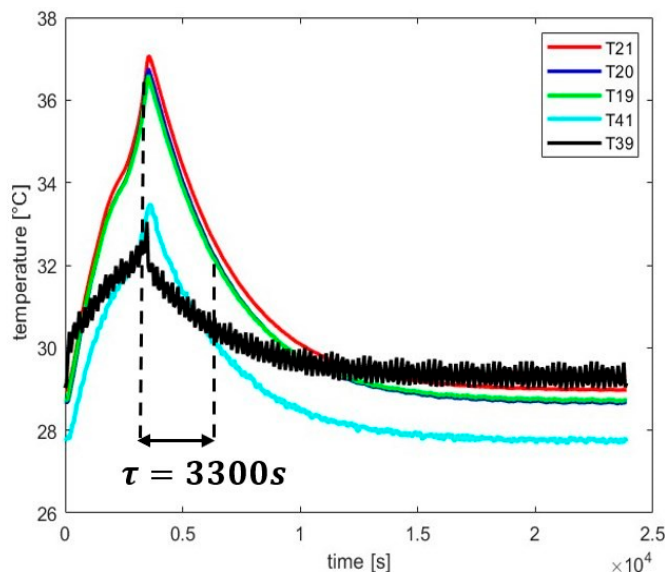


**Figure 16.** The thermal behaviour of the battery module with dual cooling while discharging.

Table 4 presents the relative uncertainties for the various measurements of the temperature, voltage, and current [32].

**Table 4.** Estimated uncertainties of measured quantities.

Measured Quantity	Unit	Uncertainty	Range
Voltage	[mV]	2	100 [V]
Current	[A]	1.5	500 [A]
Temperature	[°C]	0.9	55 [°C]

## 5. Model Validation and Extrapolations

A series of electrothermal tests were performed to verify the battery module model. However, to maintain conciseness, this paper will focus on a single test. The current profile utilized for the model validation is illustrated in Figure 16. This particular current profile was beneficial as it facilitated a thorough examination of the entire state of charge (SOC) range, thereby allowing for the validation of the lookup tables pertaining to the battery electrical resistances during both charging and discharging, in addition to the open circuit voltage (OCV). Furthermore, it allowed us to evaluate the effects of the current amplitude on the thermal and electrical responses of the batteries [33].

The experimental test conditions and certain simplifying assumptions, along with boundary conditions, were established to facilitate the simulation of the model and to compare the results obtained with those from the experiment, and are as follows:

- The module was fitted with bottom and top cooling plates;
- The air temperature was maintained at 25 °C while the coolant temperature was regulated at 20 °C;
- The initial temperature was 20.7 °C;
- A single cell within the module was selected for the purpose of comparing the model with the experimental results;
- The thermocouple used for the measurement was positioned at the center of the larger surface of this cell.

Figure 16 presents a comparison of the simulation performed with Matlab Simulink software (version 2022.b) and the experimental data in terms of the temperature response at two different locations on the battery module. T39 indicates the temperature response of sensor 39 located on the busbar, whereas T20 reflects the temperature response of thermocouple 20, which was situated at the center of the larger surface of the fourth battery from the left, as illustrated in Figure 12. Figure 17 demonstrates that the model effectively replicates the thermal behaviour at the specified locations (busbar and cell surface). Various scenarios were previously examined, incorporating different temperature and current profiles, and the model consistently exhibited its reliability by accurately capturing similar behaviours regarding temperature and voltage fluctuations. It was noted that the model's precision diminished at low state of charges (SOCs) due to unaccounted for highly non-linear phenomena that influenced the battery's behaviour under such conditions [34]. As the SOC decreased, the disparity in the temperature between the simulated and experimental outcomes progressively widened, ultimately reaching a maximum of 1.2 °C.

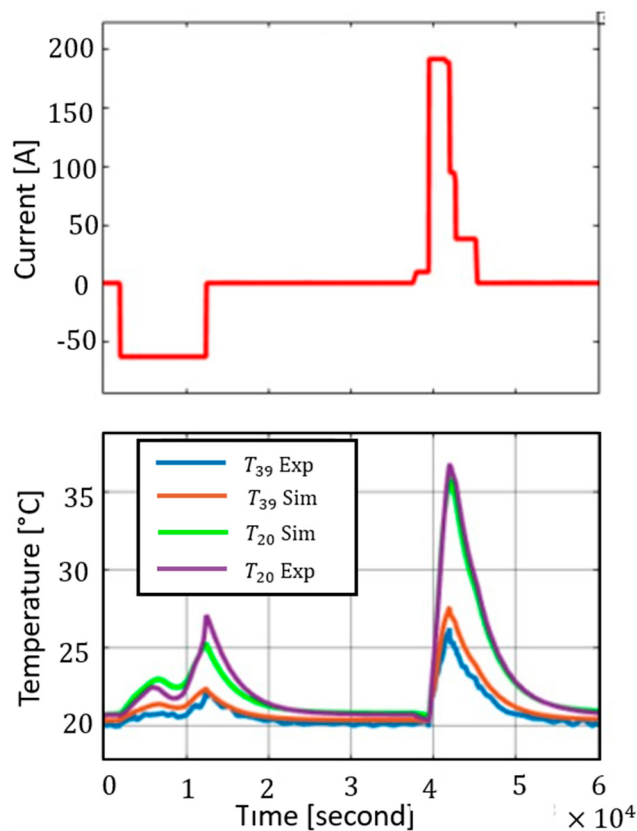


**Figure 17.** Comparison between simulation results and experimental data [23].

Even at elevated C-rates, the deviation remained less than the uncertainty attributed to the thermocouple, which was  $\pm 1.5$  °C. In summary, the model exhibited robust performance, particularly when accounting for the complexities of the battery's nonlinear behaviour and the uncertainties inherent in the experimental data.

A comparison of the three configurations illustrated in Figure 4 underscores the advantages of incorporating a top cooling plate on the busbars to enhance the thermal management of the battery module. As depicted in Figure 18, the third configuration, which includes both top and bottom cooling plates and is represented by the blue curve, demonstrates the highest efficiency in thermal management. This arrangement proves to be the most effective in extracting and dissipating the heat generated during the charging and discharging processes. Consequently, the maximum peak temperature is lowered in comparison to the configuration represented by the black curve, which utilizes only a bottom cooling plate. Additionally, the time constant is notably decreased, further validating the efficacy of this configuration [35,36].

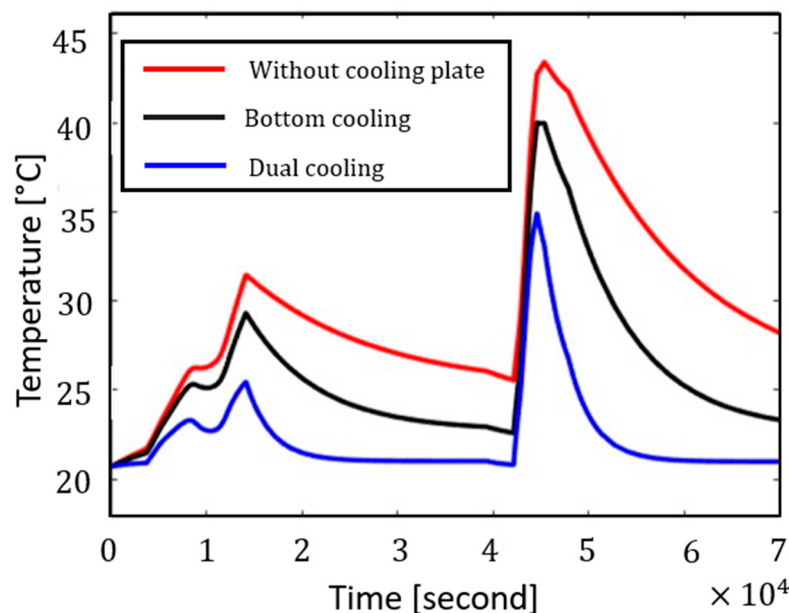


**Figure 18.** Comparative study of three different configurations [23].

This analysis was conducted utilizing the identical current profile illustrated in Figure 17, with the air temperature maintained at 25 °C and the coolant temperature established at 20 °C.

Based on the experimental and simulation results presented in Section 2, no thermal gradient is observed at the JR or cell level. This lack of gradient can be attributed to the limitation of the power source at 196 A, as well as the effective performance of the bottom cooling plate [37].

It is essential to highlight that the heat transfer coefficient for the bottom cooling plate, after model calibration, is 66 [W·m<sup>-1</sup>·K<sup>-1</sup>]. This value seems unusually low and inconsistent with the expected range for the convection coefficients of cooling plates, raising concerns about the performance of the bottom cooling plate and suggesting the need for further investigation (this can be attributed to a coolant circulation or a thermal contact problem). In contrast, the heat transfer coefficient for the top cooling plate is 500 [W m<sup>-1</sup> K<sup>-1</sup>]. It is important to note that this low value for the heat transfer coefficient for the bottom cooling plate does not impact the results presented, as the model allows us to assign any desired convection coefficient to the cooling plate, enabling us to simulate the specific scenario accordingly. For instance, the model is extended for a charge current of 3C, with the convection coefficient set at 500, 1000, and 2000 [W·m<sup>-1</sup>·K<sup>-1</sup>] for both cooling plates [38]. The results obtained are shown in Figure 19. It shows that the thermal gradients calculated using relation [17,23]

$$\Delta T = T_{\max JR} - T_{\min JR} \quad (13)$$

are, respectively, [3.2, 4.5, and 5.8] in the bottom cooling configuration and [1.8, 2.8, and 3.9] in the dual cooling configuration at the end of the charge.

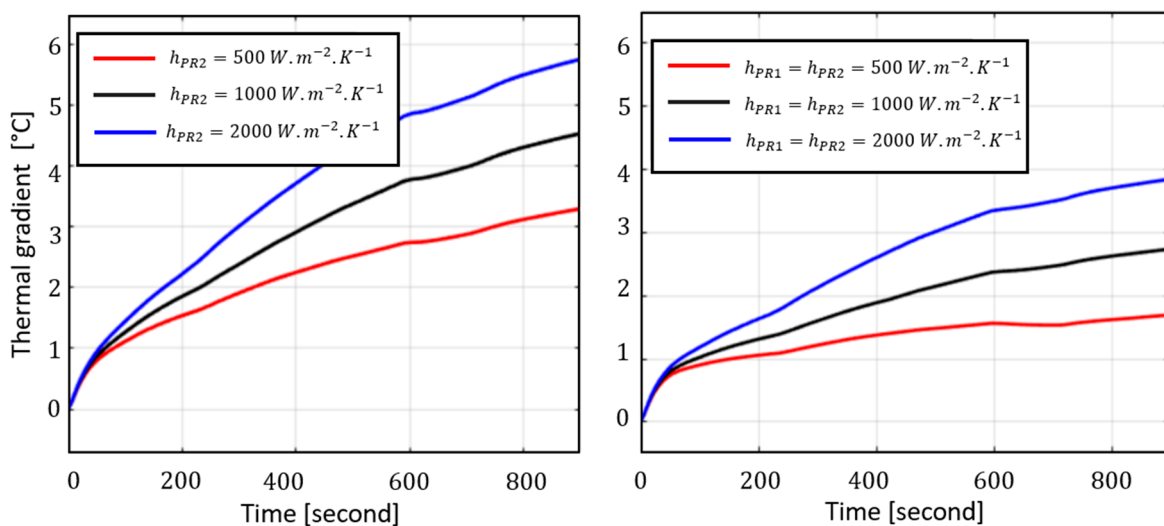


**Figure 19.** The thermal gradient obtained for the bottom cooling configuration (**left**) and dual cooling configuration (**right**) for a 3C charge with an ambient and cooling liquid temperature of 25 °C and  $SOC_{init} = 0\%$ .

## 6. Conclusions

This research presented a methodology for the modelling of battery modules, encompassing battery cells and thermal spacers placed between the cells and busbars. A qualitative evaluation was conducted on a battery module to assess the advantages of utilizing a dual cooling system. The particular case study demonstrated that the incorporation of both bottom and top cooling plates resulted in the accelerated cooling of the module. This integration led to a 47% reduction in the thermal time constant (an additional cooling surface led to a faster temperature drop within the same time frame) and a decrease of 6 °C in the maximum battery temperature when compared to a traditional cooling system. A series of electrothermal tests were performed to validate the model of the battery module across various scenarios involving different coolant and air temperatures, as well as different current profiles during both the charging and discharging phases. The model showed commendable reproducibility, with the errors remaining consistently below the uncertainty levels of the thermocouples used. Additionally, the implementation of the top cooling plate enhanced the efficiency of heat extraction from the batteries and reduced the thermal gradient inside the cell. While this study primarily addressed prismatic cells, the proposed methodology is relevant to a variety of battery types and module configurations. Nevertheless, as dual cooling distributes the cooling zones, for the same amount of energy it can largely be hoped that the thermal gradient inside a cell will be reduced compared to a solution only involving bottom cooling. Of course, this hypothesis must be verified. Future research may focus on a comparative analysis of thermal management systems, such as dual cooling and immersible cooling, with an emphasis on efficiency and energy consumption—critical factors that affect vehicle performance. Additionally, the modelling efforts detailed in this paper, which included the incorporation of an extra top cooling plate, provided the authors with the opportunity to examine the heat flow pathways through the internal connections of a cell, and to propose modifications to its dimensions to enhance cooling efficiency. This modelling work will also serve as the basis for a study investigating the benefits of a cooling plate during rapid charging phases, as well as the development of a charging profile aimed at minimizing the charging time while adhering to voltage and temperature limitations. All of this research will be discussed in a forthcoming article.

**Author Contributions:** Conceptualization, S.M., J.S., J.-M.V. and F.G.; Methodology, S.M., J.S. and J.-M.V.; Software, F.G.; Validation, B.G., R.G., Z.D. and N.A.; Resources, B.G., R.G., Z.D. and N.A.; Writing—original draft, S.M., J.S., J.-M.V. and F.G.; Writing—review & editing, S.M., J.S., J.-M.V. and F.G. All authors have read and agreed to the published version of the manuscript.

**Funding:** This work took place within the framework of OpenLab’s ‘Electronic and Systems for Automotive’, involving IMS Laboratory and Stellantis in collaboration with Lodz University of Technology. This work was carried out under a CIFRE agreement and funded by the ANRT, grant number is 2020/1011.

**Data Availability Statement:** The original contributions presented in the study are included in the article, further inquiries can be directed to the corresponding author.

**Conflicts of Interest:** Authors Said Madaoui, Zlatina Dimitrova, Nicolas Audiot and Franck Guillemand were employed by the company Stellantis. The remaining authors declare that the research was conducted in the absence of any commercial or financial relationships that could be construed as a potential conflict of interest.

### Notations

In this paper, the following notations are used.

$h_{conv}$	Heat transfer coefficient
$Q_{irr}$	Irreversible heat
$Q_{rev}$	Reversible heat
$R_{30s\ i,j}$	Electrical resistance of a mesh i, j (obtained after 30 s)
$R_{th\ CP}$	Thermal resistance attributed to the cooling plate
$R_{th\ TI}$	Thermal interface resistance
$S_{BBi}$	Cross-sectional area of the busbar
$T_A$	Air temperature
$T_b$	Busbar temperature
$T_c$	Coolant temperature
$T_{i,j}$	Temperature of a jelly roll mesh i, j
$l_{BBi}$	Length of a busbar mesh
$\Delta T$	Thermal gradient
CC	Constant current
CV	Constant voltage
$I$	Current
JR	Jelly roll
LIB	Lithium-ion battery
SOC	State of charge
$T$	Average battery temperature
$t$	Time
TMS	Thermal management system
OCV	Open circuit voltage
$S$	Convection surface
$e$	Thickness
$\rho$	Density of a material
$\tau$	Time constant (defined by the authors)

### References

- Maisel, F.; Neef, C.; Marscheider-Weidemann, F.; Nissen, N.F. A forecast on future raw material demand and recycling potential of lithium-ion batteries in electric vehicles. *Resour. Conserv. Recycl.* **2023**, *192*, 106920. [[CrossRef](#)]
- Li, S.; Zhang, C.; Zhao, Y.; Offer, G.J.; Marinescu, M. Effect of thermal gradients on inhomogeneous degradation in lithium-ion batteries. *Commun. Eng.* **2023**, *2*, 74. [[CrossRef](#)]
- Song, D.; Wang, S.; Di, L.; Zhang, W.; Wang, Q.; Wang, J.V. Lithium-Ion Battery Life Prediction Method under Thermal Gradient Conditions. *Energies* **2023**, *16*, 767. [[CrossRef](#)]
- Steinhardt, M.; Gillich, E.I.; Stiegler, M.; Jossen, A. Thermal conductivity inside prismatic lithium-ion cells with dependencies on temperature and external compression pressure. *J. Energy Storage* **2020**, *32*, 101680. [[CrossRef](#)]
- Zhou, Y.; Wang, Z.; Xie, Z.; Wang, Y. Parametric Investigation on the Performance of a Battery Thermal Management System with Immersion Cooling. *Energies* **2022**, *15*, 2554. [[CrossRef](#)]

6. Hunt, I.A.; Zhao, Y.; Patel, Y.; Offer, J. Surface Cooling Causes Accelerated Degradation Compared to Tab Cooling for Lithium-Ion Pouch Cells. *J. Electrochem. Soc.* **2016**, *163*, A1846–A1852. [[CrossRef](#)]
7. Feng, X.; Xu, C.; He, X.; Wang, L.; Zhang, G.; Ouyang, M. Mechanisms for the evolution of cell variations within a LiNi<sub>x</sub>CoyMnzO<sub>2</sub>/graphite lithium-ion battery pack caused by temperature non-uniformity. *J. Clean. Prod.* **2018**, *205*, 447–462. [[CrossRef](#)]
8. Shi, C.; Kim, S.-H.; Warren, N.; Guo, N.; Zhang, X.; Wang, Y.; Willemsen, A.; López-Pernía, C.; Liu, Y.; Kingon, A.I.; et al. Hierarchically Micro- and Nanostructured Polymer via Crystallinity Alteration for Sustainable Environmental Cooling. *Langmuir* **2024**, *40*, 20195–20203. [[CrossRef](#)]
9. Amalesh, T.; Narasimhan, N.L. Liquid cooling vs hybrid cooling for fast charging lithium-ion batteries: A comparative numerical study. *Appl. Therm. Eng.* **2022**, *208*, 118226. [[CrossRef](#)]
10. Liu, J.; Fan, Y.; Xie, Q. Feasibility study of a novel oil-immersed battery cooling system: Experiments and theoretical analysis. *Appl. Therm. Eng.* **2022**, *208*, 118251. [[CrossRef](#)]
11. Mohammed, A.H.; Esmaeeli, R.; Aliniagerdroudbari, H.; Alhadri, M.; Hashemi, S.R.; Nadkarni, G.; Farhad, S. Dual-purpose cooling plate for thermal management of prismatic lithium-ion batteries during normal operation and thermal runaway. *Appl. Therm. Eng.* **2019**, *160*, 114106. [[CrossRef](#)]
12. Wu, S.; Xiong, R.; Li, H.; Nian, V.; Ma, S. The state of the art on preheating lithium-ion batteries in cold weather. *J. Energy Storage* **2020**, *27*, 101059. [[CrossRef](#)]
13. Kalogiannis, T.; Jaguemont, J.; Omar, N.; Van Mierlo, J.; Bossche, P.V.D. A Comparison of Internal and External Preheat Methods for NMC Batteries. *World Electr. Veh. J.* **2019**, *10*, 18. [[CrossRef](#)]
14. Dao, T.-S.; Vyasarayani, C.P.; McPhee, J. Simplification and order reduction of lithium-ion battery model based on porous-electrode theory. *J. Power Sources* **2012**, *198*, 329–337. [[CrossRef](#)]
15. Wang, D.; Huang, H.; Tang, Z.; Zhang, Q.; Yang, B.; Zhang, B. A lithium-ion battery electrochemical–thermal model for a wide temperature range applications. *Electrochim. Acta* **2020**, *362*, 137118. [[CrossRef](#)]
16. Barreras, J.V.; Raj, T.; Howey, D.A. Derating Strategies for Lithium-Ion Batteries in Electric Vehicles. In Proceedings of the IECON 2018—44th Annual Conference of the IEEE Industrial Electronics Society, Washington, DC, USA, 21–23 October 2018. [[CrossRef](#)]
17. Madaoui, S.; Vinassa, J.-M.; Sabatier, J.; Guillemand, F. An Electrothermal Model of an NMC Lithium-Ion Prismatic Battery Cell for Temperature Distribution Assessment. *Batteries* **2023**, *9*, 478. [[CrossRef](#)]
18. Rezvanizaniani, S.M.; Liu, Z.; Chen, Y.; Lee, J. Review and recent advances in battery health monitoring and prognostics technologies for electric vehicle (EV) safety and mobility. *J. Power Sources* **2014**, *256*, 110–124. [[CrossRef](#)]
19. Palmieri, B.; Cilento, F.; Siviello, C.; Bertocchi, F.; Giordano, M.; Martone, A. Mitigation of Heat Propagation in a Battery Pack by Interstitial Graphite Nanoplatelet Layer: Coupled Electrochemical-Heat Transfer Model. *J. Compos. Sci.* **2022**, *6*, 296. [[CrossRef](#)]
20. Xu, X.; Zhang, H.; Cao, L.; Yi, Z.; Li, P.; Guo, H. Heat generation and surrogate model for large-capacity nickel-rich prismatic lithium-ion battery as against 18650 battery. *J. Loss Prev. Process. Ind.* **2022**, *77*, 104783. [[CrossRef](#)]
21. Wu, L.; Liu, K.; Liu, J.; Pang, H. Evaluating the heat generation characteristics of cylindrical lithium-ion battery considering the discharge rates and N/P ratio. *J. Energy Storage* **2023**, *64*, 107182. [[CrossRef](#)]
22. Gozdur, R.; Guzowski, B.; Dimitrova, Z.; Noury, A.; Mitukiewicz, G.; Batory, D. An energy balance evaluation in lithium-ion battery module under high temperature operation. *Energy Convers. Manag.* **2021**, *227*, 113565. [[CrossRef](#)]
23. Madaoui, S.; Guzowski, B.; Gozdur, R.; Dimitrova, Z.; Audiot, N.; Sabatier, J.; Vinassa, J.-M.; Guillemand, F. Evaluation of Dual Side Cooling System for Prismatic Batteries for Vehicle Applications. In Proceedings of the 36th International Conference on Efficiency, Cost, Optimization, Simulation and Environmental Impact of Energy Systems (ECOS 2023), Las Palmas de Gran Canaria, Spain, 25–30 June 2023; pp. 2218–2228.
24. Worwood, D.; Kellner, Q.; Wojtala, M.; Widanage, W.; McGlen, R.; Greenwood, D.; Marco, J. A new approach to the internal thermal management of cylindrical battery cells for automotive applications. *J. Power Sources* **2017**, *346*, 151–166. [[CrossRef](#)]
25. Fleckenstein, M.; Bohlen, O.; Bäker, B. Aging Effect of Temperature Gradients in Li-ion Cells Experimental and Simulative Investigations and the Consequences on Thermal Battery Management. *World Electr. Veh. J.* **2012**, *5*, 322–333. [[CrossRef](#)]
26. Zhang, X.; Wierzbicki, T. Characterization of plasticity and fracture of shell casing of lithium-ion cylindrical battery. *J. Power Sources* **2015**, *280*, 47–56. [[CrossRef](#)]
27. Bree, G.; Horstman, D.; Low, C.T.J. Light-weighting of battery casing for lithium-ion device energy density improvement. *J. Energy Storage* **2023**, *68*, 107852. [[CrossRef](#)]
28. Das, A.; Barai, A.; Masters, I.; Williams, D. Comparison of Tab-To-Busbar Ultrasonic Joints for Electric Vehicle Li-Ion Battery Applications. *World Electr. Veh. J.* **2019**, *10*, 55. [[CrossRef](#)]
29. Zwicker, M.; Moghadam, M.; Zhang, W.; Nielsen, C. Automotive battery pack manufacturing—A review of battery to tab joining. *J. Adv. Join. Process* **2020**, *1*, 100017. [[CrossRef](#)]
30. Wu, X.; Zhang, K.; Chen, Y.; Du, J.; Shchurov, N. Multistage fast charging optimization protocol for lithium-ion batteries based on the biogeography-based algorithm. *J. Energy Storage* **2022**, *52*, 104679. [[CrossRef](#)]
31. Allart, D. Gestion et Modélisation Électrothermique des Batteries Lithium-Ion. Ph.D. Thesis, Université de Caen Normandie, Caen, France, 2023.
32. Huang, H. A propensity-based framework for measurement uncertainty analysis. *Measurement* **2023**, *213*, 112693. [[CrossRef](#)]

33. Calearo, L.; Thingvad, A.; Ziras, C.; Marinelli, M. A methodology to model and validate electro-thermal-aging dynamics of electric vehicle battery packs. *J. Energy Storage* **2022**, *55*, 105538. [[CrossRef](#)]
34. Ji, H.; Luo, T.; Dai, L.; He, Z.; Wang, Q. Topology design of cold plates for pouch battery thermal management considering heat distribution characteristics. *Appl. Therm. Eng.* **2023**, *224*, 119940. [[CrossRef](#)]
35. Chen, Z.; Yang, S.; Pan, M.; Xu, J. Experimental investigation on thermal management of lithium-ion battery with roll bond liquid cooling plate. *Appl. Therm. Eng.* **2022**, *206*, 118106. [[CrossRef](#)]
36. Angani, A.; Kim, H.-W.; Hwang, M.-H.; Kim, E.; Kim, K.-M.; Cha, H.-R. A comparison between Zig-Zag plated hybrid parallel pipe and liquid cooling battery thermal management systems for Lithium-ion battery module. *Appl. Therm. Eng.* **2023**, *219*, 119599. [[CrossRef](#)]
37. Tardy, E.; Thivel, P.-X.; Druart, F.; Kuntz, P.; Devaux, D.; Bultel, Y. Internal temperature distribution in lithium-ion battery cell and module based on a 3D electrothermal model: An investigation of real geometry, entropy change and thermal process. *J. Energy Storage* **2023**, *64*, 107090. [[CrossRef](#)]
38. Jiang, G.; Zhuang, L.; Hu, Q.; Liu, Z.; Huang, J. An investigation of heat transfer and capacity fade in a prismatic Li-ion battery based on an electrochemical-thermal coupling model. *Appl. Therm. Eng.* **2020**, *171*, 115080. [[CrossRef](#)]

**Disclaimer/Publisher’s Note:** The statements, opinions and data contained in all publications are solely those of the individual author(s) and contributor(s) and not of MDPI and/or the editor(s). MDPI and/or the editor(s) disclaim responsibility for any injury to people or property resulting from any ideas, methods, instructions or products referred to in the content.